

Nonlinear Hall responses in tunable nodal Dirac semimetals

Akash Dey*

¹ National Institute of Science Education and Research, Jatni, Odisha 752050, India and
² Homi Bhabha National Institute, Training School Complex, Anushakti Nagar, Mumbai 400094, India
(Dated: November 26, 2025)

We investigate the nonlinear Hall responses in tunable two-dimensional Dirac materials. In particular, we study quantum geometry-driven second and third order non-linear responses in a time-reversal symmetric Dirac semimetal that can host single, double and line nodes depending on the model parameters. We find that the second-order Hall response (SOHE), which originates from the Berry curvature dipole, is enhanced in the single-node semimetallic phase as compared to the double node case when inversion symmetry is broken. In contrast, the SOHE vanishes in the nodal line semimetal as the inversion symmetry retains. Notably, the third-order Hall response due to Berry connection polarizability becomes much larger in the line-node Dirac semimetal, especially when the Fermi energy lies near the band edge, than in the single- and double-node Dirac semimetals. The reason for this contrasting behavior is attributed to the distinct distribution of the Berry connection polarizability in the Brillouin zone.

I. INTRODUCTION

In recent years, the geometry of quantum states has become crucial for understanding various unconventional electronic and optical phenomena such as photogalvanic effect, nonlinear magneto-optical responses, nonlinear Nernst effect, nonlinear Hall effect and many more [1–6]. The Berry curvature (BC), one of the key quantities that captures the geometry of quantum states, is known to drive anomalous Hall effect in systems that break time-reversal symmetry [7, 8]. Moreover, the higher-order moments of the BC, namely the Berry curvature dipole (BCD) and quadrupole (BCQ) [1, 9–11] can generate nonlinear Hall effects under different symmetry conditions. Very recently, new geometric contributions to nonlinear transport have been identified, particularly those arising from interband coherence and higher-order geometric corrections. One such quantity is the Berry connection polarizability (BCP), also referred to as the band-normalized quantum metric [12]. The BCP measures how the interband Berry connection responds to changes in energy within the band structure, providing an intrinsic mechanism for nonlinear Hall effects beyond the conventional dipole picture [13–15]. In addition, BCP is shown to serve as a probe of the Néel vector orientation [14, 16] even in PT -symmetric antiferromagnetic systems.

Dirac semimetals (DSMs) with symmetry-protected band crossings provide an excellent platform to study the effect of quantum geometry on various physical properties. Based on the dimensionality and nature of the band crossings, semimetals can be classified as Dirac [17–20], Weyl [21–24], and nodal-ring semimetals (NRSMs) [25–30]. While DSMs and Weyl semimetals (WSMs) feature discrete band-touching points, NLSMs exhibit one-dimensional crossings that form continuous loops in momentum space [31, 32]. Breaking certain symmetries can

induce transitions between these phases. For example, a DSM can transform into a WSM when either time-reversal or inversion symmetry is broken [33, 34]. In some ferromagnetic materials such as HgCr_2Se_4 , Co_2TiX ($X = \text{Si, Ge, Sn}$), and Fe_2MnX ($X = \text{P, As, Sb}$), tuning material parameters enables transitions between NLSM and WSM phases [34–37]. Beyond 3D systems, two-dimensional analogs of Dirac, Weyl, and nodal-ring semimetals have been realized in transition-metal dichalcogenides, graphene heterostructures, and mixed honeycomb–kagomé lattices [17, 38–40].

The presence of distinct nodal structures in materials are found to host distinct physical properties such as optical response[41, 42], magneto-optical transition[43], chiral anomaly induced negative magnetoresistance[44, 45], drumhead surface states and unique electromagnetic responses[46]. Motivated by the distinct properties for distinct nodal structures, we aim to understand how the geometric quantities change across these nodal points and subsequently affect the non-linear transport properties of nodal materials. To address this, we consider a low-energy model Hamiltonian of a Dirac semimetal that hosts distinct nodal structures depending on the model parameters. We then investigate how quantum geometric quantities evolve across distinct nodal phases. A family of two-dimensional semimetals, MX with $\text{M} = \text{Pd, Pt}$, and $\text{X} = \text{S, Se, Te}$ [47, 48], provides a promising platform to explore these effects. We find that BCD is significantly enhanced in the gapped single node phase as compared to the double-node phase. This behavior arises due to distinct distribution of the Berry curvatures near the nodal structure. As a result, the second order hall (SOH) response is larger in the single node phase than the double-node phase. In contrast, the SOH response vanishes in the nodal-ring phase because the Berry curvature is identically zero. However, all the three phases exhibit a non-zero third order hall (TOH) response due to the presence of nonzero BCP. Interestingly, the nodal-ring phase shows a much stronger BCP along the ring compared to the other two phases. Consequently, we ob-

* akash.dey@niser.ac.in

serve an enhanced TOH response near the band edge in the nodal-line phase, compared to the band structures with single or double nodes. This behavior can be traced back to the way BCP tensors are distributed in the Brillouin zone for the different nodal configurations. Overall, these findings provide a useful pathway to identify materials with enhanced nonlinear responses among nodal systems.

The paper is organised as follows: In Sec. III, we introduce the model Hamiltonian and the underlying symmetries. This is followed by a formal derivation for expressions for the electrically driven higher order Hall conductivities in terms of quantum geometric quantities in Sec. II. We then present numerical results showing the evolution of second-order and third-order Hall responses across various nodal phases in Section IV A and IV B. Finally, in Sec. V, we summarise our main findings and discussed about future outlook.

II. THEORETICAL BACKGROUND

We start with a general formalism to evaluate different order Hall conductivity for systems with time-reversal symmetry. Using Boltzmann transport formalism, the total electric current density is found to be

$$j_a = -e \int_k f(\mathbf{k}) \dot{\mathbf{r}}, \quad (1)$$

where e is the electron charge, $\int_k = \int d^d k / (2\pi)^d$, \mathbf{r} is the position vector of the wavepacket, and $f(\mathbf{k})$ denotes the non-equilibrium distribution function. Under the influence of an applied electric field $\mathbf{E}(t) = \text{Re}[\mathbf{E}_0 e^{i\omega t}]$, the perturbation to the system is described by $H_E = e\mathbf{E} \cdot \mathbf{r}$, which induces a position shift in the wave packet [13]. The semiclassical equations of motion, including higher-order corrections due to the electric field, can be expressed as (set $e = \hbar = 1$) [49]

$$\dot{\mathbf{r}} = \nabla_k \tilde{\epsilon}_k - \dot{\mathbf{k}} \times \tilde{\Omega}_k, \quad (2)$$

where $\hbar \dot{\mathbf{k}} = e\mathbf{E}$, $\tilde{\epsilon}_k$ and $\tilde{\Omega}_k$ are the higher-order corrections to band energy and Berry curvature, respectively. They can be expressed as

$$\tilde{\epsilon}(\mathbf{k}) = \sum_{i=0}^2 \epsilon(\mathbf{k})^{(i)}, \quad \tilde{\Omega}(\mathbf{k}) = \nabla_{\mathbf{k}} \times \sum_{i=0}^1 \mathbf{A}^{(i)}, \quad (3)$$

where $\mathbf{A}^{(i)}$ is the i -th order correction to the Berry connection. For the zeroth order correction in energy and BC, the Hall current density derived from equation (1) is given by [9, 50]:

$$j_a = \sigma_{ab} E_b + \zeta_{abc} E_b E_c. \quad (4)$$

The linear and second-order Hall conductivity σ_{ab} and ζ_{abc} respectively reads off

$$\sigma_{ab} = -\varepsilon_{abc} \int_k \Omega_c(\mathbf{k}) f_0(\mathbf{k}), \quad (5)$$

$$\zeta_{abc} = -\varepsilon_{acd} \frac{\tau}{2(1 + i\omega\tau)} D_{bd}. \quad (6)$$

Here $(a, b, c, d) \in (x, y, z)$ are applied field directions, $\partial_b = \frac{\partial}{\partial k_b}$, $f_0(\mathbf{k})$ is the equilibrium distribution function, τ is the scattering time, and ω is the driving frequency. The quantity D_{bd} in equation (6) is known as Berry curvature dipole[9] and it is defined as

$$D_{bd} = \int_k f_0(\mathbf{k}) (\partial_b \Omega_d(\mathbf{k})) = - \int_k v_b(\mathbf{k}) \Omega_d(\mathbf{k}) \frac{\partial f_0}{\partial \epsilon^{(0)}}, \quad (7)$$

where $v_b = \partial \epsilon^{(0)} / \partial k_b$ is the band velocity and the factor $\partial f_0 / \partial \epsilon^{(0)}$ restricts the integral to states near the Fermi surface at low temperature.

To capture the third-order Hall effect, we include the second-order correction to the band energy because the first-order term is gauge-dependent and vanishes in the wave-packet picture [13, 51]. We also incorporate the first-order correction to the Berry curvature. In the presence of the perturbation H_E , the first-order correction to Bloch wavefunction is

$$\langle u_{\alpha}^{(1)}(k) \rangle = \sum_{\beta \neq \alpha} \frac{e \mathbf{E} \cdot \mathbf{A}_{\beta \alpha}^{(0)} \langle u_{\beta}^{(0)}(k) \rangle}{\epsilon_{\alpha}^{(0)} - \epsilon_{\beta}^{(0)}}, \quad (8)$$

where $\mathbf{A}_{\beta \alpha}^{(0)} = \langle u_{\alpha}^{(0)}(k) | i \nabla_{\mathbf{k}} | u_{\beta}^{(0)}(k) \rangle$ is the zeroth-order interband Berry connection and α, β are the band indices. Then the first order correction in BC is $\Omega^{(1)}(k) = \nabla_{\mathbf{k}} \times \mathbf{A}^{(1)}$, where $\mathbf{A}^{(1)}$ is

$$A_{\alpha,a}^{(1)} = 2 \text{Re} \sum_{\beta \neq \alpha} \frac{A_{\alpha \beta,a}^{(0)} A_{\beta \alpha,b}^{(0)}}{\epsilon_{\alpha}^{(0)} - \epsilon_{\beta}^{(0)}} E_b = G_{\alpha,ab} E_b. \quad (9)$$

The tensor $G_{\alpha,ab}$, known as the BCP tensor, represents another key geometric quantity of the system. Moreover, the second-order correction to the band energy can be expressed in terms of this BCP tensor as follows:

$$\epsilon_{\alpha}^{(2)} = \sum_{\beta \neq \alpha} \frac{|\langle u_{\alpha}^{(0)}(\mathbf{k}) | H_E | u_{\beta}^{(0)}(\mathbf{k}) \rangle|^2}{\epsilon_{\alpha}^{(0)} - \epsilon_{\beta}^{(0)}} = \frac{1}{2} G_{ab} E_a E_b. \quad (10)$$

Next, we proceed to determine the non-equilibrium distribution function by solving the semiclassical Boltzmann equation under relaxation time approximation [52], which yields

$$\dot{\mathbf{k}} \cdot \nabla_{\mathbf{k}} f(\mathbf{k}) = \frac{f_0(\mathbf{k}) - f(\mathbf{k})}{\tau}. \quad (11)$$

For the solution of equation (11), we consider the following ansatz:

$$f(\mathbf{k}) = \sum_{n=0}^{\infty} (\tau \mathbf{E} \cdot \nabla_{\mathbf{k}})^n f_0(\tilde{\epsilon}(\mathbf{k})). \quad (12)$$

By substituting Eqs. (2) and (12) in equation (1), we

obtain the third-order current density as [15, 51, 53]

$$j^{(3)} = \int_k (\mathbf{E} \times \boldsymbol{\Omega}^{(0)}) \epsilon^{(2)} f'_0 - \tau \int_k \nabla_{\mathbf{k}} \epsilon^{(0)} (\mathbf{E} \cdot \nabla_{\mathbf{k}}) \epsilon^{(2)} f'_0 - \tau \int_k \nabla_{\mathbf{k}} \epsilon^{(2)} (\mathbf{E} \cdot \nabla_{\mathbf{k}}) f_0 + \tau \int_k (\mathbf{E} \times \boldsymbol{\Omega}^{(1)}) (\mathbf{E} \cdot \nabla_{\mathbf{k}}) f_0 + \tau^2 \int_k (\mathbf{E} \times \boldsymbol{\Omega}^{(0)}) (\mathbf{E} \cdot \nabla_{\mathbf{k}})^2 f_0 - \tau^3 \int_k \nabla_{\mathbf{k}} \epsilon^{(0)} (\mathbf{E} \cdot \nabla_{\mathbf{k}})^3 f_0. \quad (13)$$

Since both the τ -independent and τ^2 terms in right hand side of equation 13 are odd under time-reversal symmetry, neither contributes in the current density. Therefore, only the τ and τ^3 terms contribute to the third-order current and each term has a clear physical origin. The second term comes from the second-order energy correction inside the distribution function. The third term follows from the second-order field correction to the band velocity. The fourth term comes from the anomalous velocity produced by the first order field correction to the Berry curvature. The final term, which is proportional to τ^3 , originates from the band velocity and gradient of the distribution function. Since we are interested in the BCP induced TOH current, we will only consider the terms proportional to τ . Finally, we can write the TOH current density as $j_a^{(3)} = \chi_{abcd} E_b E_c E_d$, where the third order conductivity linear in τ upon simplification is given by

$$\chi_{abcd} = \tau \int_k (\partial_a \partial_b G_{cd} - \partial_a \partial_d G_{bc} + \partial_b \partial_d G_{ac}) f_0(\mathbf{k}) - \frac{\tau}{2} \int_k v_a v_b G_{cd} f''_0(\mathbf{k}). \quad (14)$$

III. MODEL HAMILTONIAN

We consider a low-energy model Hamiltonian for a two dimensional semi-metallic system[46, 47, 54, 55] as

$$H = \mathbf{d}(\mathbf{k}) \cdot \boldsymbol{\sigma}, \quad (15)$$

where $\boldsymbol{\sigma} = (\sigma_x, \sigma_y, \sigma_z)$ are the Pauli matrices acting in the pseudospin space, $\mathbf{d}(\mathbf{k}) = (d_x, d_y, d_z) = (\lambda(k^2 - k_0^2), \gamma k_y, 0)$ with $\mathbf{k} = (k_x, k_y)$, denoting the crystal momentum. Here, λ represents the inverse of the band mass, γ characterizes the Fermi velocity along the y direction and k_0 is the parameter that determines the position of the nodal points. The corresponding energy dispersion is given by

$$\epsilon_{\pm} = \pm \sqrt{(\lambda(k^2 - k_0^2))^2 + (\gamma k_y)^2}, \quad (16)$$

where \pm denote the conduction and valence bands, respectively. By tuning the parameters γ and k_0 with λ fixed, the system can be continuously driven through distinct gapless semimetallic phases, as illustrated in Fig. 1.

For $k_0 = 0$ and $\gamma \neq 0$, the two energy bands touch at a single point at $\mathbf{k} = 0$, corresponding to a single-node (SN) semimetallic phase. For both $k_0 \neq 0$ and $\gamma \neq 0$, the node splits into two distinct band-touching points at $\mathbf{k} = (\pm k_0, 0)$, leading to a double-node (DN) phase. Conversely, when $\gamma = 0$ and $k_0 \neq 0$, the discrete nodes expand into a continuous closed loop in momentum space, forming a nodal ring (NR) semimetal with a ring radius equal to k_0 . When a finite gap parameter Δ is introduced ($d_z = \Delta$), the system no longer exhibits semimetallic behavior. Nevertheless, for small values of Δ , the energy dispersion continues to reflect the underlying nodal character, with the energy bands extrema occurring near $k = 0$ and $k = k_0$ [48]. Note that for SN and DN phases, the system is invariant under mirror symmetry M_x and the discrete nodal points are located on mirror line along x direction. In contrast, in the NR phase, the system posses rotational symmetry. Note that time reversal symmetry (TRS) with $\Theta = \mathcal{K}$, where \mathcal{K} denotes the complex conjugation operator, is preserved in all three cases. However, the inversion symmetry (IS) is broken only in SN and DN phases but remains preserved in NR phase.

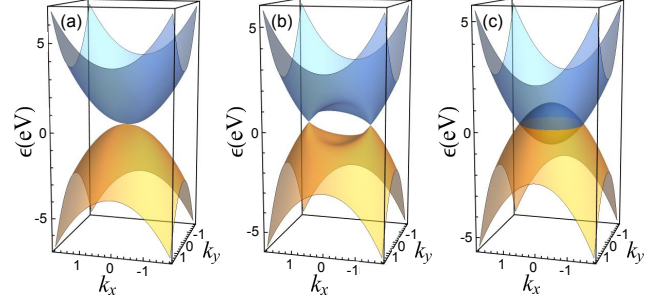


FIG. 1. Energy spectrum of Eq. 15 for different values of parameters γ and k_0 , keeping λ fixed. (a) SN phase with single nodal point at $\mathbf{k} = 0$ for $k_0 = 0$ and $\gamma = 1.0 \text{ eV} \cdot \text{\AA}$, (b) DN phase with two nodal points located at $\mathbf{k} = (\pm k_0, 0)$ for $k_0 = 1.0 \text{ \AA}^{-1}$ and $\gamma = 1 \text{ eV} \cdot \text{\AA}$, and (c) NR phase with a nodal ring of radius $k_0 = 1.0 \text{ \AA}^{-1}$ and $\gamma = 0$. Here we take $\lambda = 1.0 \text{ eV} \cdot \text{\AA}^2$ and momentum k_x, k_y are in units of \AA^{-1} .

IV. RESULTS

A. BCD induced Second order Hall effect.

The generic form of the Hamiltonian in equation 15 allow us to easily evaluate the Berry curvature as

$$\Omega_z^\pm = \frac{\mathbf{d}(\mathbf{k}) \cdot (\partial_{k_x} \mathbf{d}(\mathbf{k}) \times \partial_{k_y} \mathbf{d}(\mathbf{k}))}{2|\mathbf{d}(\mathbf{k})|^3} = \pm \frac{\lambda k_x \gamma \Delta}{[(k^2 - k_0^2)^2 \lambda^2 + k_y^2 \gamma^2 + \Delta^2]^{3/2}}. \quad (17)$$

Evidently Ω_z is an odd function of k_x . Consequently, the total BC integrated over the Brillouin zone vanishes (equation 5), ensuring that the linear Hall conductivity is zero in this time-reversal-invariant system. We therefore compute the second order conductivity arising from the BCD.

The velocity components $v_x^\pm = 2k_x d_x / \epsilon_\pm$ and $v_y^\pm = k_y(2d_x + \gamma^2) / \epsilon_\pm$, both are odd function in k_x and k_y respectively. Thus the integrand $v_x \Omega_z$ for the x component of BCD equation 7, becomes a even function under momentum inversion and contributes a finite value of D_{xz} . In contrast, for the y component, the integrand $v_y \Omega_z$ become a odd function that integrates to zero, thereby suppressing the D_{yz} . This is consistent with the underlying mirror symmetry M_x , which forbids any BCD response along y -direction [9, 56]. Importantly, this finite BCD emerges even without any explicit *tilt* in the band structure. It arises inherently from the distribution of the Berry curvature in momentum space combined with the velocity anisotropy, demonstrating that nonlinear Hall responses can exist in untilted systems when the underlying band geometry lacks complete inversion symmetry in momentum space. The magnitude and profile of this response further depend on the nodal configuration of the system as will be discussed next.

For the NR phase with $\gamma = 0$, the BC vanishes, and therefore this phase posses no second order response. We therefore focus only on the finite responses that arise in the SN and DN phases. In the SN phase, Fig. 2(a) shows the density plot of the integrand $v_x \Omega_z$. Clearly, this quantity is strongly concentrated near the origin and displays two symmetric positive regions due to k_x^2 term in the numerator, leading to a large net dipole, as seen in Fig. 2c. In contrast, in the DN phase, the integrand shown in Fig. 2(b) is concentrated around $k_x = \pm k_0$, forming a dipole-like structure with opposite signs. As a result, the net dipole contribution is significantly reduced as illustrated in Fig. 2(c). In both cases, the response vanishes in the gap region as the BCD is a Fermi surface property. Also, the response reaches to its maximum value near the band edge as BC become maximum at the band edges (see Fig. 2(d)). Note that as the Hamiltonian is TRS invariant, the BCP induced intrinsic second order Hall response is absent [57] in all these cases.

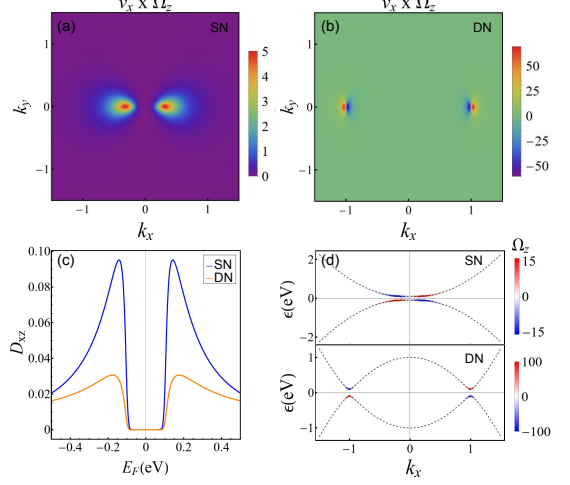


FIG. 2. (a,b) Density plots showing the Berry curvature (Ω_z) multiplied by the velocity component for the single-node and double-node phases, respectively. (c) Plot of the Berry curvature dipole D_{xz} for both these phases. Here, we take gap parameter $\Delta = 0.1$ eV. (d) Density plot of Berry curvature along the energy spectrum in the $k_y = 0$ plane for both the SN and DN phases. Here Ω_z and D_{xz} are in units of \AA^2 and \AA^3 respectively.

B. BCP induced third order Hall effect:

Since the third order Hall response is not restricted by TRS and IS [15, 51], we observe a finite BCP induced TOH response in all three phases. Using equation 9, different components of the BCP tensor for the Hamiltonian in equation 15 are found to be

$$\begin{aligned} G_{xx}^\pm &= \pm \frac{k_x^2 (k_y^2 \gamma^2 + \Delta^2) \lambda^2}{[(k^2 - k_0^2)^2 \lambda^2 + k_y^2 \gamma^2 + \Delta^2]^{5/2}}, \\ G_{yy}^\pm &= \pm \frac{\gamma^2 (\Delta^2 + (k_0^2 - k_x^2 + k_y^2)^2 \lambda^2) + 4k_y^2 \Delta^2 \lambda^2}{4 [(k^2 - k_0^2)^2 \lambda^2 + k_y^2 \gamma^2 + \Delta^2]^{5/2}}, \\ G_{xy}^\pm &= G_{yx}^\pm = \pm \frac{k_x k_y ((k_0^2 - k_x^2 + k_y^2) \gamma^2 + 2\Delta^2) \lambda^2}{2 [(k^2 - k_0^2)^2 \lambda^2 + k_y^2 \gamma^2 + \Delta^2]^{5/2}}, \end{aligned} \quad (18)$$

where \pm denote conduction and valence bands of equation (15). In Fig. 3, we have shown the density plots of these BCP tensor components across different nodal phases. Each phase develops its own characteristic BCP structure, and these differences strongly influence the corresponding third-order Hall responses. In the SN phase, one might expect a monopole like structure near $\mathbf{k} = 0$ for the diagonal components, similar to that of a single Dirac-point system [15]. However, in the present model, the G_{xx} component of the BCP displays two symmetric lobes along the k_x -axis, as shown in Fig. 3(a). As before, this feature originates from the k_x^2 factor appearing in the numerator of G_{xx} in equation 18. This in turn forces the contribution to vanish exactly at the origin.

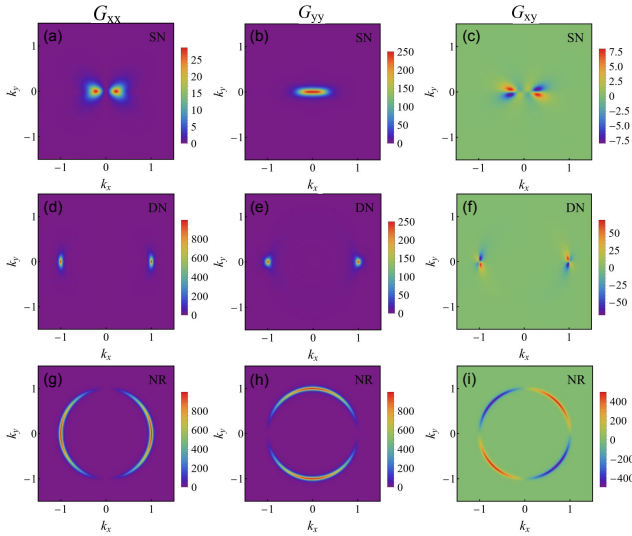


FIG. 3. Density plots of the BCP tensor components G_{xx} (left column), G_{yy} (middle column) and G_{xy} (right column) for all three phases, obtained from equation 18. The top row (a-c), middle row (d-f) and bottom row (g-i) correspond to the SN, DN and NR phases, respectively. The plots are shown only for the conduction band. Here we consider the gap $\Delta = 0.1$ eV.

However, in the immediate vicinity of the origin, the denominator becomes small, enhancing the response, leading to two symmetric maxima near $k_x=0$. In contrast, the G_{yy} and G_{xy} exhibits a monopole and a quadrupole-like structure as illustrated in Fig. 3(b) and 3(c) respectively, similar to a single Dirac-point system. Note that G_{yy} is significantly larger than both G_{xx} and G_{xy} due to constant numerator at the origin.

In the DN phase, both the diagonal components G_{xx} , G_{yy} exhibit two localized monopoles, as shown in Fig. 3(d) and 3(e) respectively. The off diagonal term G_{xy} shows two quadrupole-like patterns located at $k_x = \pm k_0$, as illustrated in Fig. 3(f). Notably, following equation 18, the G_{xx} and G_{xy} components exhibit stronger peak intensities as compared to the SN phase. This is attributed to finite numerator at nodes $k_x = \pm k_0$ as compared to the SN case with $k = 0$. In contrast, the G_{yy} component shows identical peak intensity proportional to $\gamma^2/4\Delta^3$ near $(k_y \approx 0, k_x \approx \pm k_0)$ and $(\mathbf{k} \approx 0)$ for DN and SN phase respectively.

In contrast to both the SN and DN phases, the NR phase shows a ring-like BCP pattern, reflecting the underlying nodal ring geometry, as shown in Fig 3(g-i). The

G_{xx} and G_{yy} components contain k_x^2 and k_y^2 in the numerator, which results in maximum density along k_x and k_y direction and forms two circular ridges following the ring, as illustrated in Fig 3(g) and Fig 3(h) respectively. Conversely, the G_{xy} component is proportional to $k_x k_y$, which leads to alternating density extrema in adjacent quadrants and vanishes along $k_x = 0, k_y = 0$ direction, shown in Fig 3(i). The overall magnitude of all components is larger in the NR phase because of the absence of $\gamma k_y \sigma_y$ term in the denominator, which effectively amplifies their intensity. For the G_{xx} component in both NR and DN phases, the dominant contribution arise near $k_y \approx 0$, and $k_x = \pm k_0$, where the peak magnitude is proportional to k_0^2/Δ^3 . Hence the G_{xx} component exhibits nearly identical peak intensities in both the NR and DN phases, even though the underlying geometric structures are different.

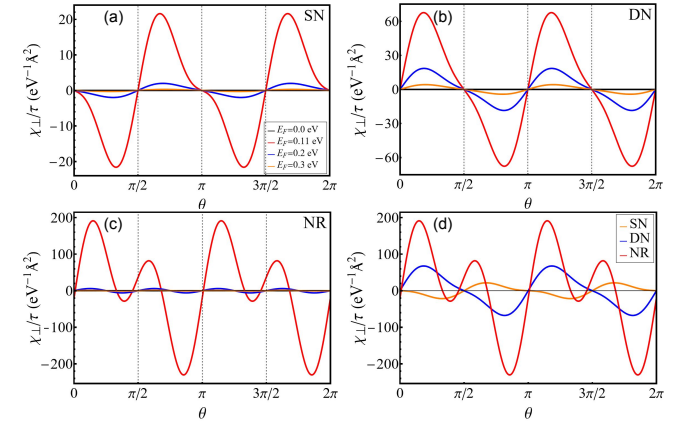


FIG. 4. The transverse TOH conductivity for different nodal phases. (a-c) shows the variation of the transverse TOH response χ_{\perp} as a function of the applied electric field direction θ for different Fermi energies E_F in the SN, DN and NR phase respectively. (d) presents the maximum transverse TOH responses together in different phases near the band edge at $E_F = 0.11$ eV. We take temperature $T=50$ K.

Using the obtained BCP tensor components, we now numerically compute the corresponding third-order conductivity tensor as defined in equation 14. In nonlinear Hall experiments, one measures the transverse current response using an in-plane electric field $\mathbf{E} = (E \cos \theta, E \sin \theta)$ oriented at an angle θ to the x-axis. Focusing on the transverse third-order Hall conductivity $\chi_{\perp}(\theta) = j_{\perp}^{(3)}/E^3$, we derive its explicit dependence on the applied electric field direction θ and obtain

$$\chi_{\perp}(\theta) = (3\chi_{21} - \chi_{11}) \sin \theta \cos^3 \theta + 3(\chi_{31} - \chi_{13}) \sin^2 \theta \cos^2 \theta + (\chi_{22} - 3\chi_{12}) \sin^3 \theta \cos \theta - \chi_{14} \sin^4 \theta + \chi_{41} \cos^4 \theta, \quad (19)$$

where $\chi_{11} = \chi_{xxxx}$, $\chi_{12} = (\chi_{xxyy} + \chi_{xyxy} + \chi_{xyyx})/3$,

$\chi_{13} = (\chi_{xxxy} + \chi_{xxyx} + \chi_{xyxx})/3$, $\chi_{14} = \chi_{xyyy}$, $\chi_{22} =$

χ_{yyyy} , $\chi_{41} = \chi_{yxxx}$, $\chi_{31} = (\chi_{yyyx} + \chi_{yyxy} + \chi_{yxyy})/3$, and $\chi_{21} = (\chi_{yyxx} + \chi_{xyyx} + \chi_{xyxy})/3$.

Note that, the SN and DN phases preserve the M_x mirror symmetry. This symmetry ensures that the tensor components involving odd number of x and y in the index (like χ_{xyyy} , χ_{yxxx}) must vanish [15, 51]. As a result, the transverse TOH conductivity χ_{\perp} vanishes when θ become integer multiples of $\pi/2$, i.e., along and perpendicular to the mirror line in Fig. 4(a) and Fig. 4(b) respectively. For both SN and DN phase, the BCP components have maximum density concentrated near the gapped nodal points. Also, there is an anisotropy in the dispersion present through $\gamma k_y \sigma_y$ term which leads to nonzero transverse TOH response [15, 51, 53]. As seen in Fig 3, the BCP components in DN phase are larger in magnitude than SN phase. Consequently, the TOH response become higher in DN phase at every values of the Fermi energy than the SN phase, as shown in Fig 4(a) and Fig 4 (b).

In the NR phase, the Fermi surface appears to be isotropic when $\gamma = 0$. But the system still shows the largest third-order transverse Hall (TOH) response near the band edge, as illustrated in Fig. 4(d). This occurs because the BCP components in the NR phase contain strongly momentum-dependent anisotropic terms such as k_x^2 , k_y^2 and $k_x k_y$ in the numerator, while the denominator has a ring-like factor $((k^2 - k_0^2)^2 \lambda^2 + \Delta^2)^{5/2}$, which peaks sharply near $k \approx k_0$. As a result the BCP distribution in momentum space becomes highly localized and anisotropic around the nodal ring. Accordingly, the individual χ_{abcd} components in the transverse conductivity χ_{\perp} does not cancel each other and gives a nonzero response. Also, in this phase, the system has rotational symmetry, which leads to all the individual TOH conductivity χ_{abcd} components to be nonzero. Consequently, the transverse conductivity χ_{\perp} does not vanish when θ become integer multiples of $\pi/2$ for all values of Fermi energy, as shown in Fig 4(c), unlikely to the other two phases. We also observe that as we move the Fermi energy far away from the band edge, the TOH responses in every phases starts diminishing as the BCP tensor are concentrated near the nodal points. For NR phase the BCP components are sharply localized along the nodal ring only, whereas for SN and DN phases the BCP components are broadly localized near the nodal points. This explains why the TOH response sharply diminish for NR

phase than other two phases if we move away from the band edges.

V. SUMMARY

We have studied the nonlinear Hall response in tunable nodal semimetals. By tuning the band parameters, we have traced the transition between single-node, double-node, and nodal-ring phases. Each phase shows a different pattern of quantum geometric quantities and a different hierarchy of nonlinear responses. As the system is TRS invariant and inversion asymmetric, both SN and DN phases exhibit the BCD-induced extrinsic second order hall responses. This response in the SN phase turns out to be larger than the DN phase as a manifestation of distinct distribution of the Berry curvature in the DN phase. For the NR phase, this quantity vanishes as the inversion symmetry is restored. We further find that the BCP becomes finite for all these cases and contribute to a nonzero third-order Hall response. We find that in the NR phase the BCP components have larger magnitude and sharply confined near the band edge along the nodal ring. These leads to an enhanced TOH response however it falls quickly as the Fermi level moves away from the band edge. It is worth pointing out that the system shows these nonlinear Hall responses inherently in all nodal phases without any tilt or warping of the Fermi surface [58]. In sum, our study highlights 2D semimetallic systems with tunable nodal phases that can be used to control quantum geometry driven transport phenomena.

VI. ACKNOWLEDGEMENT

AD thanks Kush saha and Snehasish Nandy for useful discussions. AD acknowledge financial support from the Department of Atomic Energy (DAE), Govt. of India and CSIR for giving fellowship (File No.-09/1002(0049)/2020-EMR-I).

REFERENCES:

- [1] N. Nagaosa, J. Sinova, S. Onoda, A. H. MacDonald, and N. P. Ong, Anomalous hall effect, *Rev. Mod. Phys.* **82**, 1539 (2010).
- [2] J. E. Moore and J. Orenstein, Confinement-induced berry phase and helicity-dependent photocurrents, *Phys. Rev. Lett.* **105**, 026805 (2010).
- [3] T. Morimoto, S. Zhong, J. Orenstein, and J. E. Moore, Semiclassical theory of nonlinear magneto-optical responses with applications to topological dirac/weyl semimetals, *Phys. Rev. B* **94**, 245121 (2016).
- [4] P. Törmä, Essay: Where can quantum geometry lead us?, *Phys. Rev. Lett.* **131**, 240001 (2023).
- [5] C. Zeng, S. Nandy, A. Taraphder, and S. Tewari, Nonlinear nernst effect in bilayer wte₂, *Phys. Rev. B* **100**, 245102 (2019).
- [6] D. C. Brody and L. P. Hughston, Geometric quantum mechanics, *Journal of Geometry and Physics* **38**, 19 (2001).

[7] D. Xiao, M.-C. Chang, and Q. Niu, Berry phase effects on electronic properties, *Rev. Mod. Phys.* **82**, 1959 (2010).

[8] F. D. M. Haldane, Berry curvature on the fermi surface: Anomalous hall effect as a topological fermi-liquid property, *Phys. Rev. Lett.* **93**, 206602 (2004).

[9] I. Sodemann and L. Fu, Quantum nonlinear hall effect induced by berry curvature dipole in time-reversal invariant materials, *Phys. Rev. Lett.* **115**, 216806 (2015).

[10] Z.-Y. Cao, A.-Q. Wang, X.-Y. Liu, T.-Y. Zhao, D. Yu, and Z.-M. Liao, Nonlinear hall effect and scaling law analysis in twisted bilayer WSe₂, *Phys. Rev. B* **111**, 125407 (2025).

[11] M. Huang, Z. Wu, J. Hu, X. Cai, E. Li, L. An, X. Feng, Z. Ye, N. Lin, K. T. Law, and N. Wang, Giant nonlinear hall effect in twisted bilayer wse₂, *National Science Review* **10**, nwac232 (2022), <https://academic.oup.com/nsr/article-pdf/10/4/nwac232/50268204/nwac232.pdf>.

[12] G. Sala, M. T. Mercaldo, K. Domi, S. Gariglio, M. Cuoco, C. Ortix, and A. D. Caviglia, The quantum metric of electrons with spin-momentum locking, arXiv preprint arXiv:2407.06659 (2024).

[13] Y. Gao, S. A. Yang, and Q. Niu, Field induced positional shift of bloch electrons and its dynamical implications, *Phys. Rev. Lett.* **112**, 166601 (2014).

[14] H. Liu, J. Zhao, Y.-X. Huang, W. Wu, X.-L. Sheng, C. Xiao, and S. A. Yang, Intrinsic second-order anomalous hall effect and its application in compensated anti-ferromagnets, *Phys. Rev. Lett.* **127**, 277202 (2021).

[15] H. Liu, J. Zhao, Y.-X. Huang, X. Feng, C. Xiao, W. Wu, S. Lai, W.-b. Gao, and S. A. Yang, Berry connection polarizability tensor and third-order hall effect, *Phys. Rev. B* **105**, 045118 (2022).

[16] C. Wang, Y. Gao, and D. Xiao, Intrinsic nonlinear hall effect in antiferromagnetic tetragonal cumnas, *Phys. Rev. Lett.* **127**, 277201 (2021).

[17] S. M. Young and C. L. Kane, Dirac semimetals in two dimensions, *Phys. Rev. Lett.* **115**, 126803 (2015).

[18] S. Borisenko, Q. Gibson, D. Evtushinsky, V. Zabolotnyy, B. Büchner, and R. J. Cava, Experimental realization of a three-dimensional dirac semimetal, *Phys. Rev. Lett.* **113**, 027603 (2014).

[19] L. Liu, C.-M. Miao, Q.-F. Sun, and Y.-T. Zhang, Two-dimensional dirac semimetals with tunable edge states, *Phys. Rev. B* **110**, 245413 (2024).

[20] D. Swain, A. Dey, A. Roy, K. Saha, and S. D. Das, Nontrivial phonon dynamics and significant electron-phonon coupling of the high-frequency modes in a dirac semimetal, *Phys. Rev. B* **111**, 035143 (2025).

[21] A. A. Soluyanov, D. Gresch, Z. Wang, Q. Wu, M. Troyer, X. Dai, and B. A. Bernevig, Type-ii weyl semimetals, *Nature* **527**, 495 (2015).

[22] L. Lu, Z. Wang, D. Ye, L. Ran, L. Fu, J. D. Joannopoulos, and M. Soljačić, Experimental observation of weyl points, *Science* **349**, 622 (2015), <https://www.science.org/doi/pdf/10.1126/science.aaa9273>.

[23] X. Wan, A. M. Turner, A. Vishwanath, and S. Y. Savrasov, Topological semimetal and fermi-arc surface states in the electronic structure of pyrochlore iridates, *Phys. Rev. B* **83**, 205101 (2011).

[24] Q. Lu, P. S. Reddy, H. Jeon, A. R. Mazza, M. Brahlek, W. Wu, S. A. Yang, J. Cook, C. Conner, X. Zhang, *et al.*, Realization of a two-dimensional weyl semimetal and topological fermi strings, *Nature communications* **15**, 6001 (2024).

[25] C. Fang, Y. Chen, H.-Y. Kee, and L. Fu, Topological nodal line semimetals with and without spin-orbital coupling, *Phys. Rev. B* **92**, 081201 (2015).

[26] S. Xue, M. Wang, Y. Li, S. Zhang, X. Jia, J. Zhou, Y. Shi, X. Zhu, Y. Yao, and J. Guo, Observation of nodal-line plasmons in zrsis, *Phys. Rev. Lett.* **127**, 186802 (2021).

[27] P.-Y. Chang, Nodal-line semimetals and their variance, *Materials Today Quantum* **8**, 100057 (2025).

[28] X. Hu, Proximity-induced superconductivity and andreev reflection on the surface of nodal weyl semimetals, *Europhysics Letters* **149**, 56001 (2025).

[29] M.-J. Gao and J.-H. An, Engineering rich two-dimensional higher-order topological phases by flux and periodic driving, *Phys. Rev. B* **108**, L241402 (2023).

[30] L. Jin, X. Zhang, Y. Liu, X. Dai, X. Shen, L. Wang, and G. Liu, Two-dimensional weyl nodal-line semimetal in a d^0 ferromagnetic k₂N monolayer with a high curie temperature, *Phys. Rev. B* **102**, 125118 (2020).

[31] N. P. Armitage, E. J. Mele, and A. Vishwanath, Weyl and dirac semimetals in three-dimensional solids, *Rev. Mod. Phys.* **90**, 015001 (2018).

[32] C.-K. Chiu, J. C. Y. Teo, A. P. Schnyder, and S. Ryu, Classification of topological quantum matter with symmetries, *Rev. Mod. Phys.* **88**, 035005 (2016).

[33] S.-Y. Yang, H. Yang, E. Derunova, S. S. Parkin, B. Yan, and M. N. Ali, Symmetry demanded topological nodal-line materials, *Advances in Physics: X* **3**, 1414631 (2018).

[34] J. Li, H. Wang, and H. Pan, Tunable topological phase transition from nodal-line semimetal to weyl semimetal by breaking symmetry, *Phys. Rev. B* **104**, 235136 (2021).

[35] G. Xu, H. Weng, Z. Wang, X. Dai, and Z. Fang, Chern semimetal and the quantized anomalous hall effect in hgcr₂se₄, *Phys. Rev. Lett.* **107**, 186806 (2011).

[36] G. Chang, S.-Y. Xu, H. Zheng, B. Singh, C.-H. Hsu, G. Bian, N. Alidoust, I. Belopolski, D. S. Sanchez, S. Zhang, *et al.*, Room-temperature magnetic topological weyl fermion and nodal line semimetal states in half-metallic heusler co2tix (x= si, ge, or sn), *Scientific reports* **6**, 38839 (2016).

[37] J. Noky, Q. Xu, C. Felser, and Y. Sun, Large anomalous hall and nernst effects from nodal line symmetry breaking in fe₂Mnx (x = p, as, sb), *Phys. Rev. B* **99**, 165117 (2019).

[38] M. Ezawa, Second-order topological insulators and loop-nodal semimetals in transition metal dichalcogenides xte2 (x= mo, w), *Scientific reports* **9**, 5286 (2019).

[39] H. Chen, S. Zhang, W. Jiang, C. Zhang, H. Guo, Z. Liu, Z. Wang, F. Liu, and X. Niu, Prediction of two-dimensional nodal-line semimetals in a carbon nitride covalent network, *Journal of Materials Chemistry A* **6**, 11252 (2018).

[40] J.-L. Lu, W. Luo, X.-Y. Li, S.-Q. Yang, J.-X. Cao, X.-G. Gong, and H.-J. Xiang, Two-dimensional node-line semimetals in a honeycomb-kagome lattice*, *Chinese Physics Letters* **34**, 057302 (2017).

[41] Y. Shao, Z. Sun, Y. Wang, C. Xu, R. Sankar, A. J. Breindel, C. Cao, M. M. Fogler, A. J. Millis, F. Chou, Z. Li, T. Timusk, M. B. Maple, and D. N. Basov, Optical signatures of dirac nodal lines in nbasjsub₂l₂l₂, *Proceedings of the National Academy of Sciences* **116**, 1168 (2019), <https://www.pnas.org/doi/pdf/10.1073/pnas.1809631115>.

- [42] C. H. Lee, H. H. Yap, T. Tai, G. Xu, X. Zhang, and J. Gong, Enhanced higher harmonic generation from nodal topology, *Phys. Rev. B* **102**, 035138 (2020).
- [43] J. Jeon, T. Kim, J. Jang, H. Kim, M. Ozerov, J. S. Kim, H. Min, and E. Choi, Unveiling three types of fermions in a nodal ring topological semimetal through magneto-optical transitions, *Phys. Rev. Lett.* **135**, 086901 (2025).
- [44] X. Huang, L. Zhao, Y. Long, P. Wang, D. Chen, Z. Yang, H. Liang, M. Xue, H. Weng, Z. Fang, X. Dai, and G. Chen, Observation of the chiral-anomaly-induced negative magnetoresistance in 3d weyl semimetal taas, *Phys. Rev. X* **5**, 031023 (2015).
- [45] F. Balduini, A. Molinari, L. Rocchino, V. Hasse, C. Felser, M. Sousa, C. Zota, H. Schmid, A. G. Grushin, and B. Gotsmann, Intrinsic negative magnetoresistance from the chiral anomaly of multifold fermions, *Nature Communications* **15**, 6526 (2024).
- [46] P.-Y. Chang, *Nodal-line semimetals and their variance* (2025), arXiv:2507.02329 [cond-mat.str-el].
- [47] Y.-J. Jin, R. Wang, J.-Z. Zhao, Y.-P. Du, C.-D. Zheng, L.-Y. Gan, J.-F. Liu, H. Xu, and S. Tong, The prediction of a family group of two-dimensional node-line semimetals, *Nanoscale* **9**, 13112 (2017).
- [48] S. Barati, H. Rahimpoor, and S. H. Abedinpour, Quantum hall effect and optical magnetoconductivity of two-dimensional topological nodal-line semimetals, *Phys. Rev. B* **111**, 075125 (2025).
- [49] Y. Gao, S. A. Yang, and Q. Niu, Geometrical effects in orbital magnetic susceptibility, *Phys. Rev. B* **91**, 214405 (2015).
- [50] A. Bandyopadhyay, N. B. Joseph, and A. Narayan, Non-linear hall effects: Mechanisms and materials, *Materials Today Electronics* **8**, 100101 (2024).
- [51] T. Nag, S. K. Das, C. Zeng, and S. Nandy, Third-order hall effect in the surface states of a topological insulator, *Phys. Rev. B* **107**, 245141 (2023).
- [52] N. W. Ashcroft and N. Mermin, *Solid state*, Physics (New York: Holt, Rinehart and Winston) Appendix C (1976).
- [53] O. Pal and T. K. Ghosh, Polarization and third-order hall effect in iii-v semiconductor heterojunctions, *Phys. Rev. B* **109**, 035202 (2024).
- [54] H. Rahimpoor and S. H. Abedinpour, Collective excitations and screening in two-dimensional tilted nodal-line semimetals, *Phys. Rev. B* **109**, 045120 (2024).
- [55] V. Pandey, D. Joy, D. Culcer, and P. Bhalla, Longitudinal dc conductivity in dirac nodal line semimetals: Intrinsic and extrinsic contributions, *Phys. Rev. B* **110**, 155108 (2024).
- [56] A. Bandyopadhyay, N. B. Joseph, and A. Narayan, Berry curvature dipole and its strain engineering in layered phosphorene, *Materials Today Electronics* **6**, 100076 (2023).
- [57] K. Das, S. Lahiri, R. B. Atencia, D. Culcer, and A. Agarwal, Intrinsic nonlinear conductivities induced by the quantum metric, *Phys. Rev. B* **108**, L201405 (2023).
- [58] S. S. Samal, S. Nandy, and K. Saha, Nonlinear transport without spin-orbit coupling or warping in two-dimensional dirac semimetals, *Phys. Rev. B* **103**, L201202 (2021).